CrossMark

ORIGINAL ARTICLE

A gas-liquid-solid three-phase abrasive flow processing method based on bubble collapsing

Jiang-qin Ge[1] · Shi-ming Ji[1] · Da-peng Tan[1,2]

© Springer-Verlag London Ltd. 2017

Abstract Soft abrasive flow (SAF) processing presents advantages in avoiding surface damages and adapting complex workpiece shapes. However, the current SAF method exhibits low processing efficiency for materials. To solve this problem, a gas-liquid-solid three-phase abrasive flow processing method (GLSP) based on bubble collapsing is proposed. Through a surface constrained module, a multi-inlet constrained flow passage for silicon wafer processing is constructed, in which the bubbles are injected into the abrasive flow to strengthen the processing efficiency. On the basis of the Euler multi-phase model and population balance model (PBM), a GLSP fluid mechanic model is set up. Simulation results show that the bubble collapse region can be controlled by designing the flow passage structure and that the near-wall particle turbulent motion can be strengthened by decreasing the fluid viscosity. The observation and processing experiments show that the most violent bubble collapsing occurs in the initial constrained surface region. Bubble collapsing can result in an average particle velocity increase from 12.90 to 15.97 m/s. The proposed GLSP method can increase the processing efficiency by 50% compared with the SAF method, and the average surface roughness can reach 2.84 nm.

Keywords Gas-liquid-solid three-phase abrasive flow · Bubble collapsing · Hard-brittle material · Processing efficiency · Population balance model

✉ Da-peng Tan
tandapeng@zjut.edu.cn

[1] Key Laboratory of E&M, Ministry of Education & Zhejiang Province, Zhejiang University of Technology, Hangzhou 310014, China

[2] State Key Laboratory of Digital Manufacturing Equipment & Technology, Wuhan 430074, China

1 Introduction

Monocrystalline silicon, optical glass, and functional ceramic are typical hard-brittle materials and are widely applied in the precise device manufacturing involved in modern optics, electronic information, and thin film science [1–5]. The surface quality of precise devices determines their reliabilities and performances; therefore, it is essential to perform the precision processing on the surfaces of various precise devices.

According to the differences in processing principles, the current precision processing methods for hard-brittle materials can be divided into two categories: tool-contact processing and fluid-based processing. The irregular scratches and surface damages in the former method are easily created if the grinding force is non-uniform, especially when the sizes of abrasive particles and impurities are inconsistent [6–11]. Meanwhile, the fluid in the latter method drives the particles to impact on the workpiece surface and the intensity of particle-wall collision is soft. When a particle with large size contacts with the workpiece, the fluid can buffer the over-impacting effects and the deep scratches and surface repeated damages can be reduced.

The fluid-based processing methods mainly involve magnetorheological finishing (MRF) [12], abrasive flow machining (AFM) [13], elastic emission machining (EEM) [14], and different types of jet processing methods, such as abrasive water jet (AWJ) [15] or magnetorheological jet polishing (MJP) [16]. MRF and EEM can obtain extremely high precision surface and do not result in subsurface damage. AFM needs to construct enclosed space on the workpiece and is particularly suited for the processing of curved pipe. Jet processing methods can realize deterministic processing of complex cavity surface characterized by large length-diameter ratio. When working on workpieces with irregular geometric shape surfaces, such as curved holes, helical grooves, thin

🍸 Springer

slots, or large curvature passages, the above-mentioned methods are hard to satisfy the expected technical requirements. Consequently, a no-tool processing method, the so-called soft abrasive flow (SAF) processing, is put forward [17]. During the course of SAF processing, one or several mechanical constrained modules are covered on the surface of workpiece and an enclosed and re-circulating flow passage can be constructed. The fluid medium of SAF is of low viscosity and high flow velocity. Therefore, SAF can easily generate the turbulent flow state, which can improve the surface quality and adapt complex geometric shapes.

SAF processing has been researched and applied in many engineering fields, such as micro-electro-mechanical components, precise molds, and complex titanium alloy surfaces, because of its technical advantages. Ji et al. adopted the discrete phase model (DPM) to set up the dynamic model oriented to SAF, and the processing mechanism of SAF was revealed. Their simulation results showed that the near-wall particle trajectories are disordered and that a uniform surface quality is obtained [18]. According to the Nikuradse's experimental principles, Li et al. studied the motion regulars of SAF and acquired the friction coefficient formulas suited for SAF processing. Their experimental results showed that SAF method can increase mold structural surface precision more than 10 times [19]. Zhang et al. used SAF processing to process titanium alloy artificial joints and validated the effectiveness and feasibility of this method by particle image velocimetry (PIV) [20]. Tan et al. addressed the processing non-uniformity problem and improved the surface quality of single-inlet SAF processing by introducing the fluid collision theory into the fluid-based processing area and proposing a double-inlet constrained passage. Their experimental results showed that the average roughness on the parallel flowing direction processed by the double-inlet apparatus is less than 50 nm and that the roughness curves show good convergence [21].

From the above-mentioned references, it can be inferred that the SAF processing method can cover irregular geometric surfaces and possess larger effective processing region. The particle kinetic energy is provided mainly by pump, and the flow passage structure can significantly influence the near-wall particle turbulent motion. Owing to the restrictions of flow passage structure and pump power, the current SAF method exhibits low processing efficiency, especially on hard-brittle materials. In addition, further strengthening the near-wall particle turbulent motion can improve the processing quality.

Related researches have suggested that gas bubbles may collapse under certain conditions, such as intensive pressure fluctuation, high turbulent disturbance, and multi-phase fluid collision [22–24]. The collapse of a large number of bubbles can generate innumerable micro-jets [25, 26], which can strengthen the local flow velocity and turbulent kinetic energy. In this study, bubbles are continuously injected into the SAF

to utilize the positive effects of bubble collapsing. Furthermore, an improved fluid-based processing method for the hard-brittle materials, namely, the gas-liquid-solid three-phase abrasive flow processing method (GLSP), is proposed. The bubble collapsing region can be controlled by designing the flow passage structure and regulating the flow field profiles. According to the Preston equation, the kinetic energy of particles is the key factor of material removal rate and the randomness movement of particles is a necessary condition to obtain a uniform surface texture. Under the effects of bubble collapsing, the kinetic energy of particles can be enhanced and the movement can be highly disordered.

Apparently, the solution of gas-liquid-solid three-phase flow field and the validation of bubble injection effect are the key scientific tasks of the paper. To address the above-mentioned goals, the corresponding research procedures are conducted as follows. First, on the basis of Euler multi-phase model and population balance model (PBM), a GLSP fluid mechanical model is set up. Accordingly, the preliminary flow field characteristics and the bubble collapsing distribution are acquired. On this basis, the optimal control parameters can be obtained. Then, the simulation results for three-phase abrasive flow field can be validated and the motion regulars and collapsing evolution process of bubbles can be revealed using the PIV method. Finally, a GLSP processing experimental platform is developed, and the processing experiments for silicon wafer are performed to check the effectiveness of the proposed method.

This paper is organized as follows. In Section 2, the working principle of GLSP method is presented. In Section 3, the GLSP fluid mechanic model is set up. In Section 4, the boundary conditions of the GLSP flow passage are described and the numerical simulations for the flow field characteristics of the constrained passage are performed. In Section 5, a PIV-based observation platform is established and the observation results are analyzed. In Section 6, a GLSP experimental platform is developed, and the experiments are implemented. In Section 7, the conclusions are presented.

2 Working principle and fluid mechanic model of GLSP

The flow medium of GLSP is the gas-liquid-solid three-phase abrasive flow with weak viscosity, in which the gas phase contains large number of millimeter-size bubbles. First, the liquid and the abrasive particles are mixed in advance (particle concentration is approximately 10%) and the two-phase flow medium is created. Then, the two-phase flow medium and the gas are respectively pumped into a valve, thereby creating the flow medium of GLSP (gas volume fraction is approximately 15%). After being mixed together, the three-phase flow medium is injected into the inlets of the processing tool, as shown in Fig. 1. Three brushes of abrasive flow from three inlets
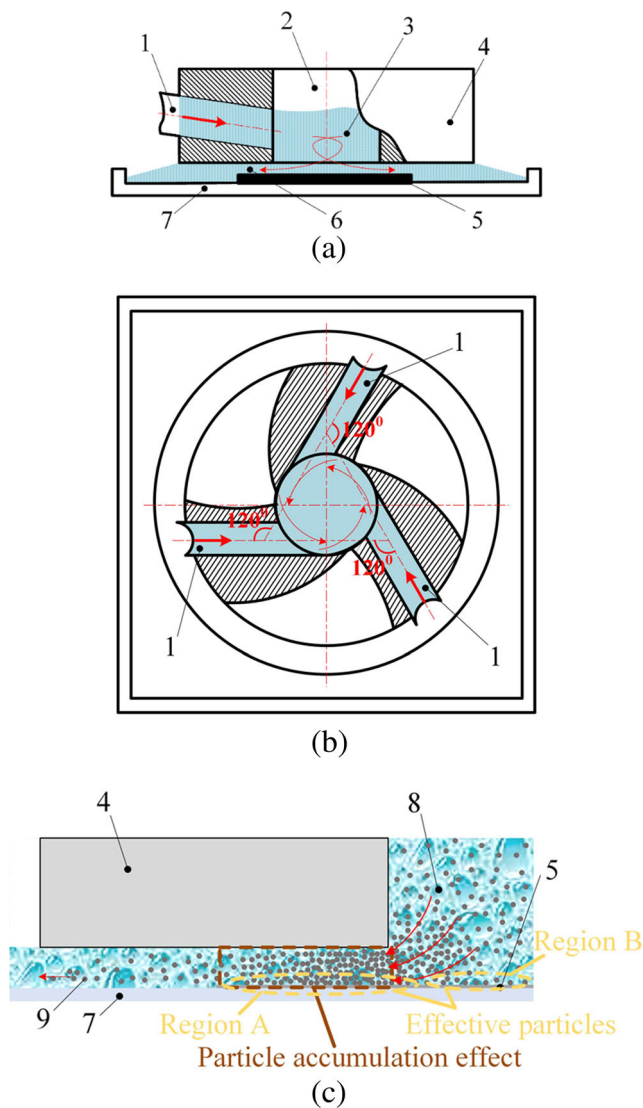
Fig. 1 Abridged view of GLSP method. **a** Orthogonal view of processing tool. **b** Vertical view of processing tool. **c** Constrained physical space structure: 1 inlet, 2 non-constrained space, 3 gas-liquid-solid three-phase abrasive flow, 4 constrained module, 5 workpiece, 6 constrained flow passage, 7 fixture, 8 bubbles, 9 abrasive particle

converge together in a non-constrained space, in which a Rankine vortex is created by the fluid collision effects (Fig. 1b). At the same time, the bubbles will collapse owing to the fluid collision and the movements of abrasive particles will become highly disordered. Finally, the mixed three-phase abrasive flow enters into the constrained space, and the velocity reaches its maximum. The workpiece surface is processed by the continuous particle-wall plow effects. When the abrasive flow enters into constrained space, a large number of bubbles will collapse violently because of turbulent vortex, and as a result, the particle motion will be enhanced.

From the above-mentioned processing principle, we can find that the constrained flow passage, multi-directional abrasive flow injection, and the bubble injection are the three key technological factors of GLSP. As shown in Fig. 1c, setting the constrained flow passage can form the particle accumulation effect, which will increase the number of effective processing particles. Before entering into the constrained flow passage, the effective processing particles locate mainly in region B and are in a small amount. After entering into constrained flow passage, the effective processing particles locate in region A and the amount of it increases apparently.

The abrasive flow injecting from three different directions can effectively promote the formation of turbulent vortex in the constrained space, which can in turn increase the motion randomness of particles and bubbles. Bubble injection mainly aims to further improve the processing capabilities of particles. When a large number of bubbles collapse in a finite physical space, the innumerable micro-jets will appear. Accordingly, the kinetic energy and the disorder motion of particles in the near-wall region can be strengthened.

2.1 Flow field control equations

According to the mechanical structure and working mode of GLSP method, the research objective of this paper is the three-phase fluid in a finite physical space and it should be described by a multi-phase model. Euler multi-phase model can accurately simulate the three-phase flow and the interaction among the three phases through calculating the governing equations of each phase [27–29]. The continuity and momentum equation of phase p are expressed as follows:

$$\frac{\partial}{\partial t}\left(\alpha_p \rho_p\right) + \nabla \cdot \left(\alpha_p \rho_p \boldsymbol{v}_p\right) = \sum_{p=1}^{n} \dot{m}_{pq} \tag{1}$$

$$\frac{\partial}{\partial t}\left(\alpha_p \rho_p \boldsymbol{v}_p\right) + \nabla \cdot \left(\alpha_p \rho_p \boldsymbol{v}_p \boldsymbol{v}_p\right) = -\alpha_p \nabla p_p + \nabla \cdot \overline{\overline{\boldsymbol{\tau}}}_p \tag{2}$$
$$+ \sum_{q=1}^{n} \left(\boldsymbol{R}_{pq} + \dot{m}_{pq} \boldsymbol{v}_{pq}\right) + \alpha_{pq} \rho_{pq} \boldsymbol{F}$$

where $\boldsymbol{F} = \boldsymbol{F}_p + \boldsymbol{F}_{\text{lif},p} + \boldsymbol{F}_{\text{vm},p}$, α_p, and ρ_p are the volume fraction and fluid density of the phase p respectively, $\boldsymbol{v}_p$ is the velocity of the phase p, $\dot{m}_{pq}$ is the mass transfer from the phase p to phase q, $\boldsymbol{R}_{pq}$ is the interacting force between two phases, p_p is the pressure, $\boldsymbol{v}_{pq}$ is the relative velocity between the phase p and q, $\boldsymbol{F}_p$ is the external body force, and $\boldsymbol{F}_{\text{lif},p}$ is the lift force acting on the phase q by phase p:

$$\boldsymbol{F}_{\text{lif},p} = -0.5 \rho_p \alpha_q \left|\boldsymbol{v}_p - \boldsymbol{v}_q\right| \times \left(\nabla \times \boldsymbol{v}_p\right) \tag{3}$$

$\boldsymbol{F}_{\text{vm},p}$ is the virtual mass force acting on the phase q by phase p:

$$\boldsymbol{F}_{\text{vm},p} = 0.5 \rho_p \alpha_q \left(\frac{\mathrm{d}\left(p \boldsymbol{v}_p\right)}{\mathrm{d}t} - \frac{\mathrm{d}\left(q \boldsymbol{v}_q\right)}{\mathrm{d}t}\right) \tag{4}$$

$\overline{\overline{\tau}}_p$ is the stress-strain tensor and is given as:

$$\overline{\overline{\tau}}_p = \alpha_p \mu_p \left(\nabla \boldsymbol{v}_p + \nabla \boldsymbol{v}_p^{\mathrm{T}} \right) + \alpha_p \left(\lambda_p - \frac{2}{3} \mu_p \right) \nabla \cdot \boldsymbol{v}_p \boldsymbol{I} \tag{5}$$

where λ_p is the volume viscosity and $\boldsymbol{I}$ is the turbulent intensity.

As indicated in Section 1, GLSP possesses similar physical characters to SAF, including low viscosity, high flow velocity, and constrained space. Thus, GLSP easily evolves into turbulent flow. According to the Reynolds equation:

$$\boldsymbol{Re} = \rho_{\mathrm{L}} \mathrm{v}_{\mathrm{L}} d / \mu_{\mathrm{L}}$$

where ρ_{L} and v_{L} are the density and velocity of fluid, μ_{L} is the fluid dynamic viscosity, d is the hydraulic diameter, and the minimum Reynolds number of GLSP ($Re \geq 6506$) is larger than the threshold Reynolds number of turbulence. Accordingly, the turbulence can be judged as a fully developed one, and the turbulence model should be considered in the control equations. As a classical turbulence model, the standard k-ε model has been used in a few industrial fields owing to its reliable robustness. Therefore, the standard k-ε turbulence model is adopted to describe the turbulent motion of three-phase abrasive flow:

$$\rho_{\mathrm{L}} \frac{dk}{dt} = \frac{\partial}{\partial x_i} \left[\left(\mu + \frac{\mu_t}{\sigma_k} \right) \frac{\partial k}{\partial x_i} \right] + G_k + G_b - \rho\varepsilon - Y_{\mathrm{M}} \tag{6}$$

$$\rho_{\mathrm{L}} \frac{d\varepsilon}{dt} = \frac{\partial}{\partial x_i} \left[\left(\mu + \frac{\mu_t}{\sigma_\varepsilon} \right) \frac{\partial \varepsilon}{\partial x_i} \right] + C_{1\varepsilon} \frac{\varepsilon}{k} (G_k + C_{3\varepsilon} G_b) - C_{2\varepsilon} \rho \frac{\varepsilon^2}{k} \tag{7}$$

where σ_k and σ_ε are the Prandtl number of the turbulent kinetic energy k and dissipation rate ε, respectively, G_k is the turbulent kinetic energy caused by the average velocity gradient, G_b is the turbulent kinetic energy caused by buoyancy, Y_{M} is the total dissipation rate affected by the compressible turbulent pulsation, μ is the molecular viscosity coefficient, μ_t is the turbulent viscosity coefficient, and can be solved by $\mu_t = \rho C_\mu k^2 / \varepsilon$. The other empirical parameters used in this paper are as follows: $C_{1\varepsilon} = 1.44$, $C_{2\varepsilon} = 1.92$, $C_{3\varepsilon} = 0.09$, $\sigma_k = 1.0$, and $\sigma_\varepsilon = 1.3$ [18, 19].

Using the above-mentioned models, the flow field profiles can be acquired, such as dynamic pressure, abrasive volume fraction, and turbulent kinetic energy. However, given that the bubble size is assumed to be of a constant value, the above models cannot be used to calculate the bubble collapsing process. To address this matter, PBM is introduced into the fluid mechanic model of GLSP.

2.2 GLSP-PBM

In the process of GLSP, bubble collapsing will occur ceaselessly under the effect of fluid turbulent motion and will strengthen the particle motion capacity. The distribution of the bubble collapsing on workpiece surface can reveal the

effective processing region. Bubble collapsing may create small bubbles, and the PBM can be used to describe the bubble size distribution after collapsing or aggregation [30]. Therefore, the bubble collapsing region can be acquired by use of the bubble size distribution.

In this study, the discretization PBM model is adopted and is defined as Eq. 8. The model is based on the continuous bubble size distribution in terms of discrete size groups. The bubbles of GLSP are assumed to be spherical in shape. The sizes of collapsed bubbles are discretized into six groups to show the collapse and aggregation. The volume ratio between two groups is discretized as $V_{i+1}/V_i = 2$, and the governing equation of bubble group i is:

$$\frac{\partial}{\partial t} \left(\rho_g \alpha_i \right) + \nabla \cdot \left(\rho_g \boldsymbol{u}_i \alpha_i \right) = \rho_g V_i \left(B_{\mathrm{ag},i} - D_{\mathrm{ag},i} + B_{\mathrm{br},i} - D_{\mathrm{br},i} \right) \tag{8}$$

where ρ_g is the density of the gas, $\boldsymbol{u}_i$ and α_i are the local velocity and volume fraction of bubble group i, and α_i is defined as:

$$\alpha_i = V_i N_i(\mathrm{t}) = V_i \int_{V_i}^{V_{i+1}} n(V, t) dV, i = 0, 1, \cdots, N-1 \tag{9}$$

where $n(V, t)dV$ is the number of bubbles that the volume is from V to $(V + dV)$ at time t and $B_{\mathrm{ag},i}$ and $D_{\mathrm{ag},i}$ are the birth rate and death rate of bubble group i owing to aggregation and are defined as follows:

$$B_{ag,i} = \sum_{k=1}^{N} \sum_{j=1}^{N} a\left(V_k, V_j\right) N_k(t) N_j(t) x_{kj} \xi_{kj} \tag{10}$$

$$D_{ag,i} = \sum_{j=1}^{N} a\left(V_i, V_j\right) N_i(t) N_j(t) \tag{11}$$

where N is the number of bubble groups, $a(V_i, V_j)$ is the aggregation kernel between the bubble of volume V_i and the bubble of volume V_j, and ξ_{kj} is given by:

$$\xi_{kj} = \begin{cases} 1 & \text{for } V_i < V_{ag} < V_{i+1}, (i \leq N-1) \\ 0 & \text{otherwise} \end{cases} \tag{12}$$

V_{ag} is the bubble volume resulting from the aggregation of bubble k and j and is defined as:

$$V_{ag} = \left[x_{kj} V_i + (1 - x_{kj}) V_{i+1} \right] \tag{13}$$

where x_{kj} can be estimated by:

$$x_{kj} = \frac{V_{ag} - V_{i+1}}{V_i - V_{i+1}} \tag{14}$$

$B_{\mathrm{br},i}$ and $D_{\mathrm{br},i}$ are the birth rate and death rate of the bubble group i owing to bubble collapsing:

$$B_{br,i} = \sum_{j=i+1}^{N} g\left(V_j\right) N_j(\mathrm{t}) \beta\left(V_i | V_j\right) \tag{15}$$

$$D_{\mathrm{br},i} = g(V_i)N_i(\mathrm{t}) \tag{16}$$

where $g(V_i)$ is the collapse frequency, and $\beta(V_i|V_j)$ is the probability density function of bubble collapsing from volume V_j to the bubble of volume V_i.

To solve Eq. 8, the parameters of bubble aggregation kernel $a(V_i, V_j)$, bubble collapse frequency $g(V_i)$, and probability density function $\beta(V_i|V_j)$ need to be obtained. For the GLSP method, the fluid turbulent motion is the main cause for the disorderly movement of abrasive particles and is also the key factor of the aggregation and collapsing of bubbles. Accordingly, the Luo model that mainly considers the effects of turbulent motion is adopted to calculate the above-mentioned three functions [31]. Subsequently, the volume fraction of bubble group i (α_i) can be obtained. In this way, the five other groups of volume fractions can be calculated. On the basis of the aforementioned results, the volume fraction distributions of differently sized bubbles are acquired and the bubble collapsing regions on the workpiece can be solved.

3 Numerical simulations and parameter optimization

3.1 Constrained flow passage model and mesh generation

Regarding the proposed GLSP method, a constrained flow passage physical model is set up, as shown in Fig. 2. The bottom surface of the model is the workpiece surface, and the gas-liquid-solid three-phase abrasive flow is injected into three inlets continuously and flows out from the passage outlet.

On the basis of the flow passage model, a finite element model can be built (Fig. 3). The finite element model is the discretization of physical model, and the quality of meshes determines the simulation accuracy. Concerning the flow passage model of GLSP, a large velocity gradient occurs while the abrasive flow enters into the constrained space. Therefore, mesh encryption method must be conducted in the interface of constrained and non-constrained spaces, as shown in Fig. 3d. Owing to the large structural scale variation in flow passage, tetrahedral mesh with improved adaptive is adopted to obtain enhanced mesh quality at the interfaces and the number of meshes is set at 498,637.

3.2 Boundary conditions

During the course of GLSP, the bubble and the abrasive flows are continuously supplied by air and liquid pumps. In order to obtain stable processing effect, the flow rate must be steady. If the fluid resistance loss is neglected, then the injection velocities of bubble and abrasive flows
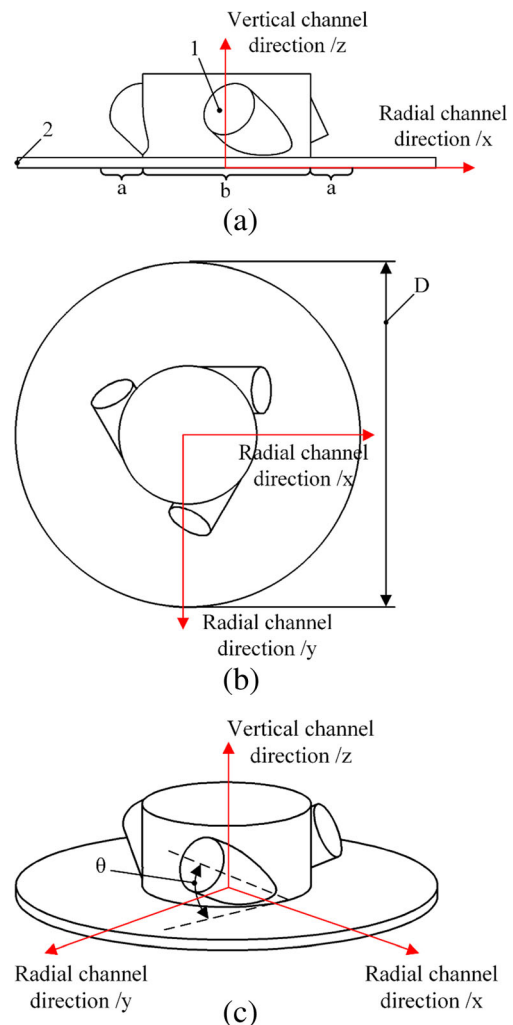

Fig. 2 GLSP flow passage model. **a** Orthogonal view. **b** Vertical view. **c** Axis view: 1 inlet, 2 outlet; $D = 200$ mm, $\theta = 27°$. *a* initial constrained surface, *b* non-constrained surface

can be calculated in accordance with the flow rate and hydraulic diameter.

On the basis of the above-mentioned hypothesis, the boundary conditions are described as follows: the inlet condition is velocity inlet, the outlet condition is outflow, the wall condition is no-slip boundary condition, the diameter of inlet is 27 mm, the distance between the processing tool and workpiece is 5 mm, the abrasive particle is SiO_2, the abrasive concentration is 10%, and the particle diameter is 10 μm. Other numerical parameters are listed in Table 1.

The fluid dynamic viscosity of GLSP is the research object in this paper and will be analyzed in Section 3.3. Semi-implicit method for pressure-linked equations (SIMPLE) algorithm and standard algorithm are adopted to deal with the pressure-velocity coupling and pressure discrete interpolation. A finite volume method based on first-order upwind scheme is used to discretize the momentum, turbulent kinetic energy, and turbulent dissipation rate.

Fig. 3 Mesh generation and boundary conditions. **a** Orthogonal view. **b** Section view of B-B side. **c** Vertical view. **d** Local enlarged view of A region. 1 velocity inlet, 2 outflow, 3 wall
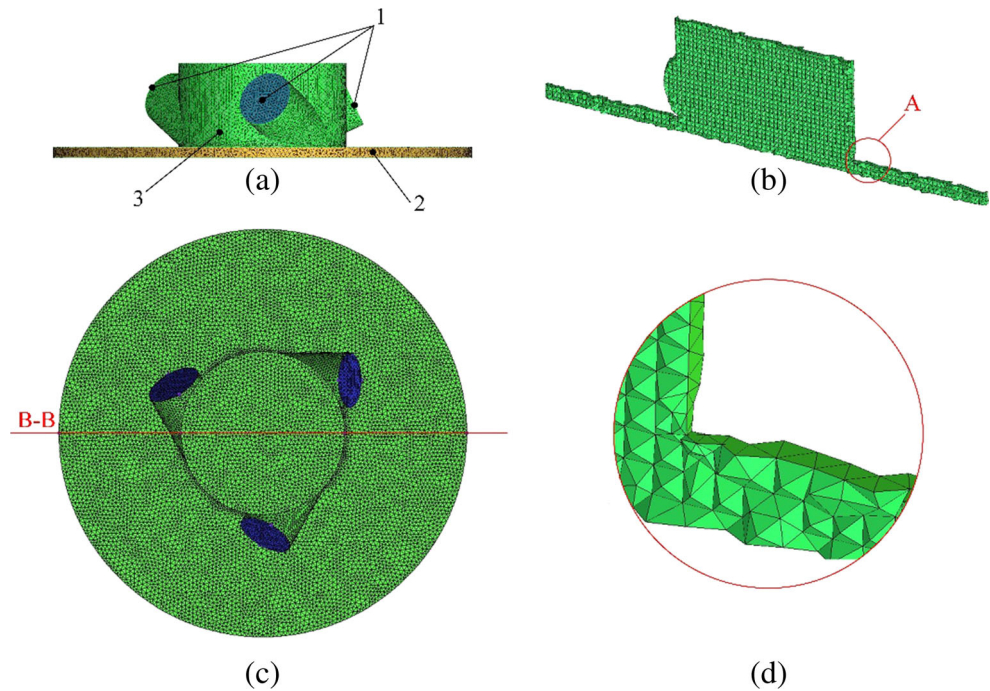
3.3 Numerical results and discussion

3.3.1 GLSP flow field characteristics

Numerical analysis of three-phase flow field in flow passage can offer useful references to the optimization of GLSP technical procedures. According to the Preston equation, abrasive particle volume fraction, granular pressure, and particle dynamic pressure are the three key factors of processing efficiency. The turbulence can characterize the intensity of particle movement and the uniformity of workpiece surface texture can be improved through increasing the turbulent kinetic energy [7, 19]. Accordingly, the numerical analysis in this paper mainly conducted around the above-mentioned four key factors.

Figure 4 shows the flow field profiles of GLSP on the workpiece surface ($u_l = 0.001$ kg/m s). The processing effect that locates in the initial constrained surface is evident, and the effective processing surface is an annular shape. Figure 4aa describes the near-wall granular pressure profile. We can find that the high granular pressure remains in the initial

Table 1 Physical parameters of GLSP

Parameters	Values
Abrasive flow injection rate (m/s)	10
Bubble injection rate (m/s)	5
Initial bubble diameter/m	0.003
Fluid dynamic viscosity (kg/m s)	u_l

constrained surface and decreases rapidly as the abrasive particles flow outward. Figure 4b presents the particle dynamic pressure profile on the workpiece. According to the dynamic pressure formula, the particle dynamic pressure profile should be similar with that of velocity. Owing to the sharp decrease in hydraulic diameter, the particle velocities increase rapidly as particles flow into the constrained space. Subsequently, the velocities decrease gradually under the effect of flow resistance. Figure 4c shows the particle volume fraction profile of GLSP. It can be found that there are a large number of abrasive particles in the initial constrained surface. The above-mentioned phenomenon indicates that the particle accumulation effect is quite evident due to the decrease of flow passage scale. Moreover, the positive effect can increase the number of effective processing particles, thereby improving the processing efficiency. As indicated above, turbulence is an important feature of GLSP. The turbulent motion of abrasive particles can improve the processing randomness, and the particle turbulent kinetic energy can reflect the turbulent motion intensity. Figure 4d shows the particle turbulent kinetic energy profile on the workpiece. We can find that the most disordered motion of abrasive particles also occurs in the initial region of constrained surface.
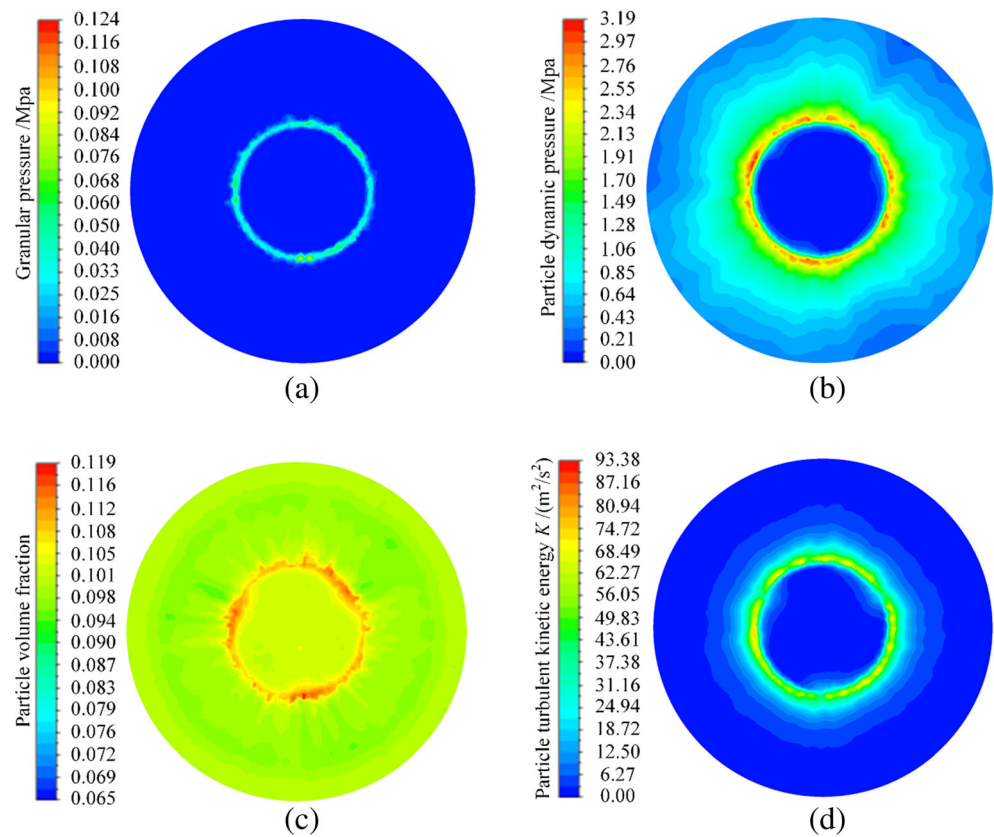
3.3.2 Bubble collapsing profiles

Innumerable micro-jets will appear when a large number of bubbles collapse and can improve the processing capability of three-phase abrasive flow. Therefore, it is necessary to obtain the bubble collapsing profiles.

Fig. 4 Flow field profiles on the surface of workpiece. **a** Granular pressure. **b** Particle dynamic pressure. **c** Particle volume fraction. **d** Particle turbulent kinetic energy

The volume fraction profiles of the differently scaled bubbles created by collapsing or aggregation are shown in Fig. 5. As mentioned in PBM theory, the sizes of collapsed bubbles are discretized into six groups to describe the bubble collapsing regions. The groups are arranged according to the magnitude of bubble size, in the following sequence: group 0 > group 1 > group 2 > group 3 > group 4 > group 5. Notably, group 0 bubbles are the initial injected bubbles.

From Fig. 5a–f, the following regulars can be inferred. (a) Owing to the bubble collapsing and aggregation, differently scaled bubbles locate in different near-wall regions. Accordingly, the collapsing and aggregation regions can be confirmed. (b) In the center region of workpiece surface, group 1 fraction presents the highest value among those of other groups. The phenomenon indicates that group 0 bubbles mainly collapse into group 1 bubbles and that the initial bubble collapsing occurs in this region. (c) As shown in Fig. 5a–f, distinct low bubble volume fraction regions locate in the initial constrained surface. On the contrary, group 5 fraction is larger than 0.9 in the same region, as shown in Fig. 5f. The above results show that the collapse of a large number of bubbles generates small bubbles (group 5) in the initial constrained surface. In other words, the most violent collapsing occurs in this region.

Combined with the simulation results of flow field profiles, the following regulars can be obtained. (a) For the flow passage model, the effective processing region locates in the initial constrained surface. Decreasing the hydraulic diameter not only can strengthen the processing capability but also can improve the processing uniformity of workpiece surface texture. (b) Two positive effects are observed after injecting the bubble flow. On the one hand, the bubble flow can disturb the flow field and reduce the flow resistance. As a result, the four key factors which are the measurements of processing capability can be strengthened. On the other hand, the violent bubble collapsing in the initial constrained surface can further improve the intensity of particle movement and increase the processing capability.

3.3.3 Numerical simulations about different fluid viscosities

According to Nikuradse's experiment principle [19] for studying the delamination of turbulence in circular tube, high Reynolds number is necessary to obtain a stable turbulent flow in a smooth wall. Given that the initial workpiece surface roughness is with a low value of approximately 0.5 μm, stable near-wall turbulence can be obtained by decreasing the fluid viscosity. For this research, six different fluid viscosities are selected in performing comparative simulation analysis (u_l = 0.015, 0.012, 0.009, 0.006, 0.003, 0.001 kg/m s). The data in the radial channel positions (the x direction in Fig. 2a) are extracted, as shown in Fig. 6.

Fig. 5 Bubble collapsing fraction profiles on the surface of workpiece. **a** Group 0. **b** Group 1. **c** Group 2. **d** Group 3. **e** Group 4. **f** Group 5
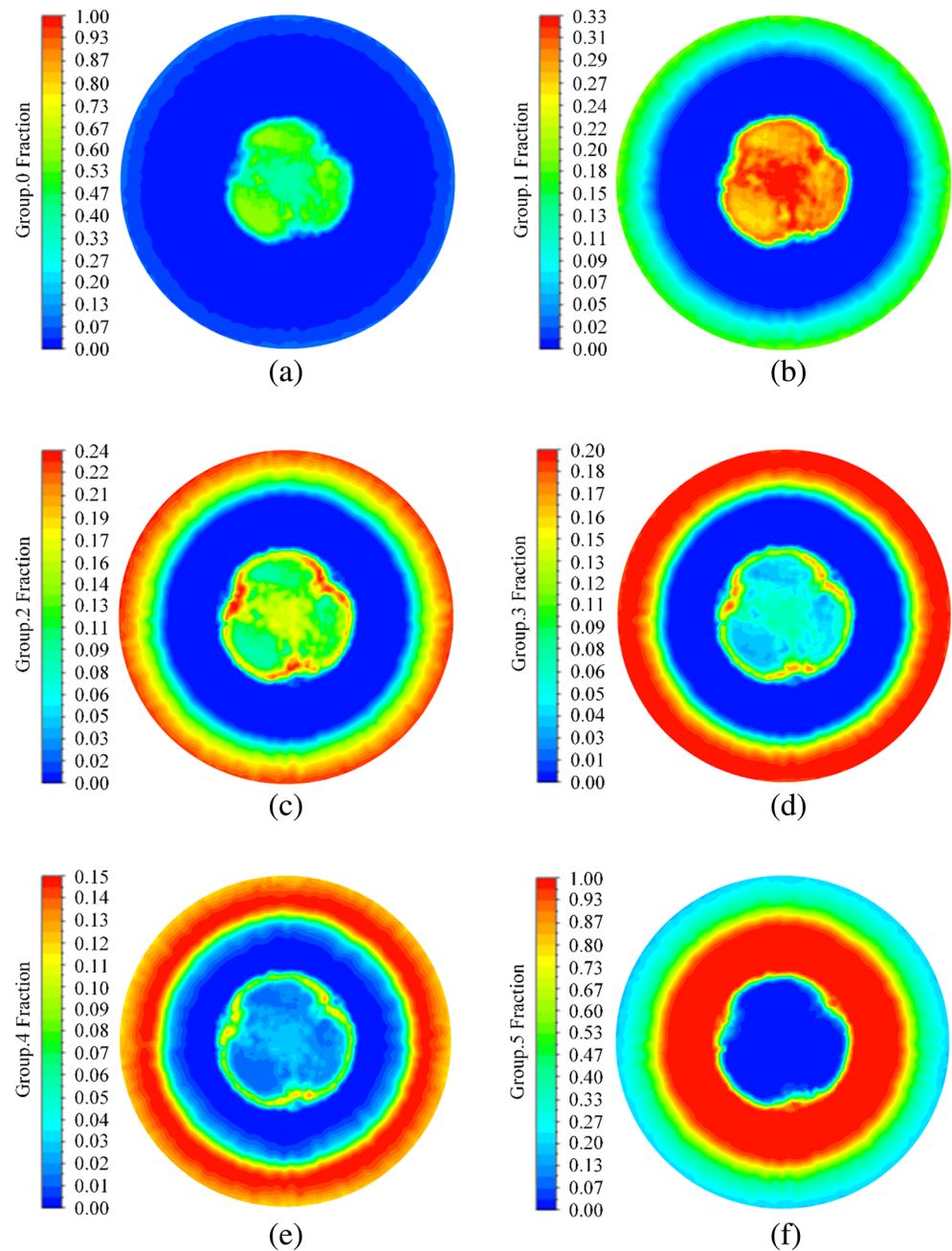
Figure 6 shows that the processing capability can be improved by decreasing the fluid viscosity. Figure 6a shows the distribution of the granular pressure. As shown in the figure, the granular pressure in the initial constrained surface is improved significantly with the decreases in fluid viscosity. The abrasive particle volume fraction increases as fluid viscosity decreases, as is shown in Fig. 6b. Meanwhile, it can be found in Fig. 6c that the particle dynamic pressure actually changes slightly with the variation in fluid viscosity. The aforementioned results can be explained by near-wall turbulent motion theory. Owing to the decreases in fluid viscosity, the flow passage viscous resistance decreases apparently, which in turn reduces the turbulent

dissipation rate (Fig. 6d). As a result, the inhibition effect on the abrasive particles becomes weak and the particle vertical motion becomes intense, which in turn enhances the granular pressure. Accordingly, the capability of fluid-transporting particles becomes weak, which in turn causes the particle accumulation in the non-constrained surface. Such accumulation increases the number of effective processing particles.

Furthermore, the effect of fluid viscosity on the bubble collapsing should be considered, and the results are shown in Fig. 7.

Figure 7a shows the bubble fraction distribution along the radial channel direction. It can be found that a large number of
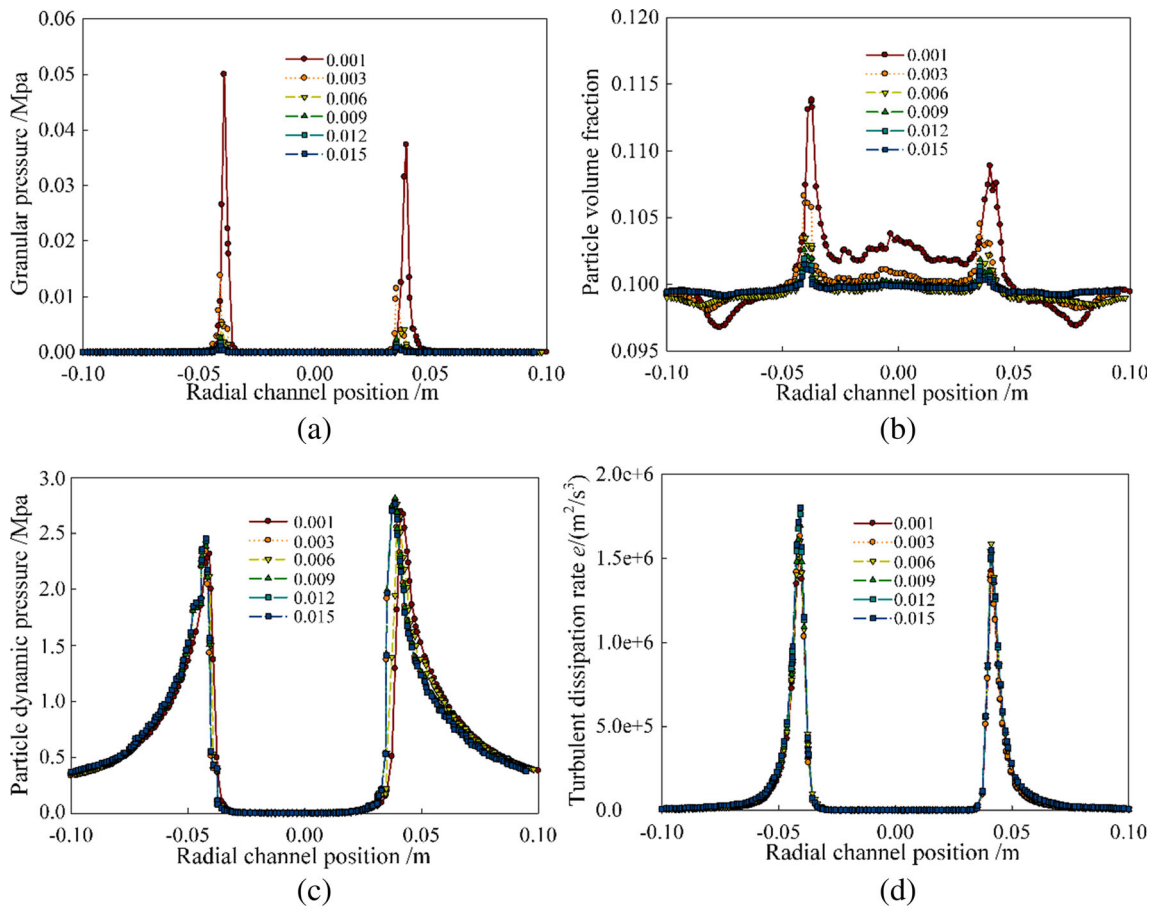
Fig. 6 Comparative results of different fluid viscosities. **a** Granular pressure. **b** Particle dynamic pressure. **c** Particle volume fraction. **d** Turbulent dissipation rate

group 5 bubbles are created in the initial constrained surface, which indicates that the bubble collapsing in this region is violent (also can be showed in Fig. 5). Figure 7b shows the bubble fraction distribution of group 5 under the condition of different viscosities. We can find that the group 5 bubble fractions are nearly the same as those in the initial constrained surface. Regarding the GLSP flow passage model, this

illustrates that the variation in fluid viscosity has not apparently impact on the bubble collapsing. As bubbles move out, the group 5 bubbles aggregate into the large bubbles and its fraction decreases. Meanwhile, the aggregation effect becomes intense with the decrease in fluid viscosity. This finding indicates that the bubble-bubble collision becomes violent with the decrease in fluid viscosity. The above results reveal that
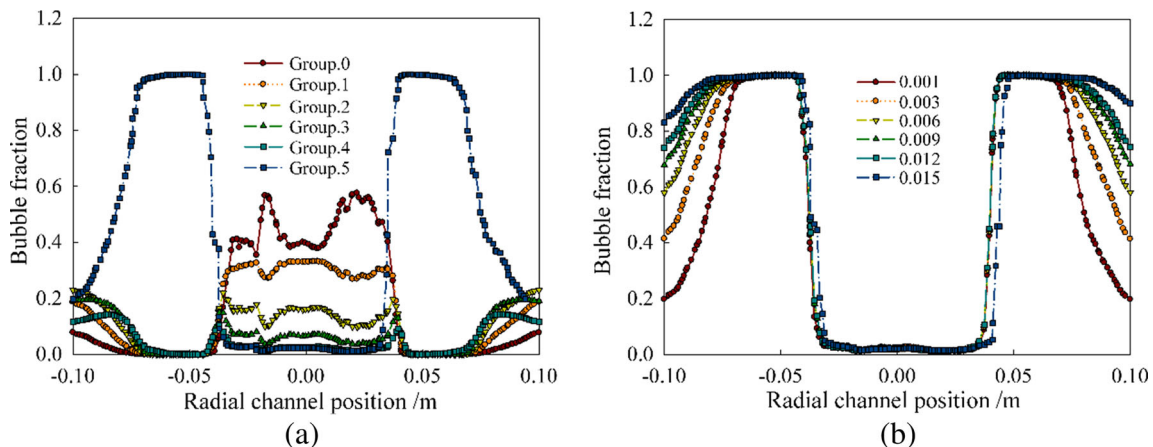

Fig. 7 Variation curves of bubble fraction. **a** Bubble group fraction with a viscosity of 0.001 kg/m s. **b** Group 5 bubble fraction of different viscosities

the near-wall particle turbulent motion can be strengthened by decreasing the fluid viscosity.

4 PIV observation experiments and result discussion

PIV is an effective observation technique in experimental fluid mechanics. The instantaneous velocity vector field can be acquired by tracking the displacement of tracer particles [32]. To obtain the reality velocity vector profile of GLSP, and verify the effectiveness of the proposed method, the PIV observation experiments are performed. The observation experiments mainly verify two targets: the flow field of GLSP and the effect of bubble collapsing.

To obtain the real-time flow field data of GLSP, a constrained flow passage physical model that is made of transparent acrylic material is developed for the PIV observation experiments, as shown in Fig. 8a1, b1. In addition, referring to the fluid-flowing similarity principle, the observation boundary conditions are consistent with the simulation boundary conditions. The experimental temperature is approximately 20 °C, and the fluid dynamic viscosity is 0.001 kg/m s. The

Fig. 8 Vertical view of the GLSP flow field. **a1** Photograph without bubble injection. **b1** Photograph with bubble injection. **a2** Average velocity vector without bubble injection. **b2** Average velocity vector with bubble injection. **a3** Vorticity profile without bubble injection. **b3** Vorticity profile with bubble injection
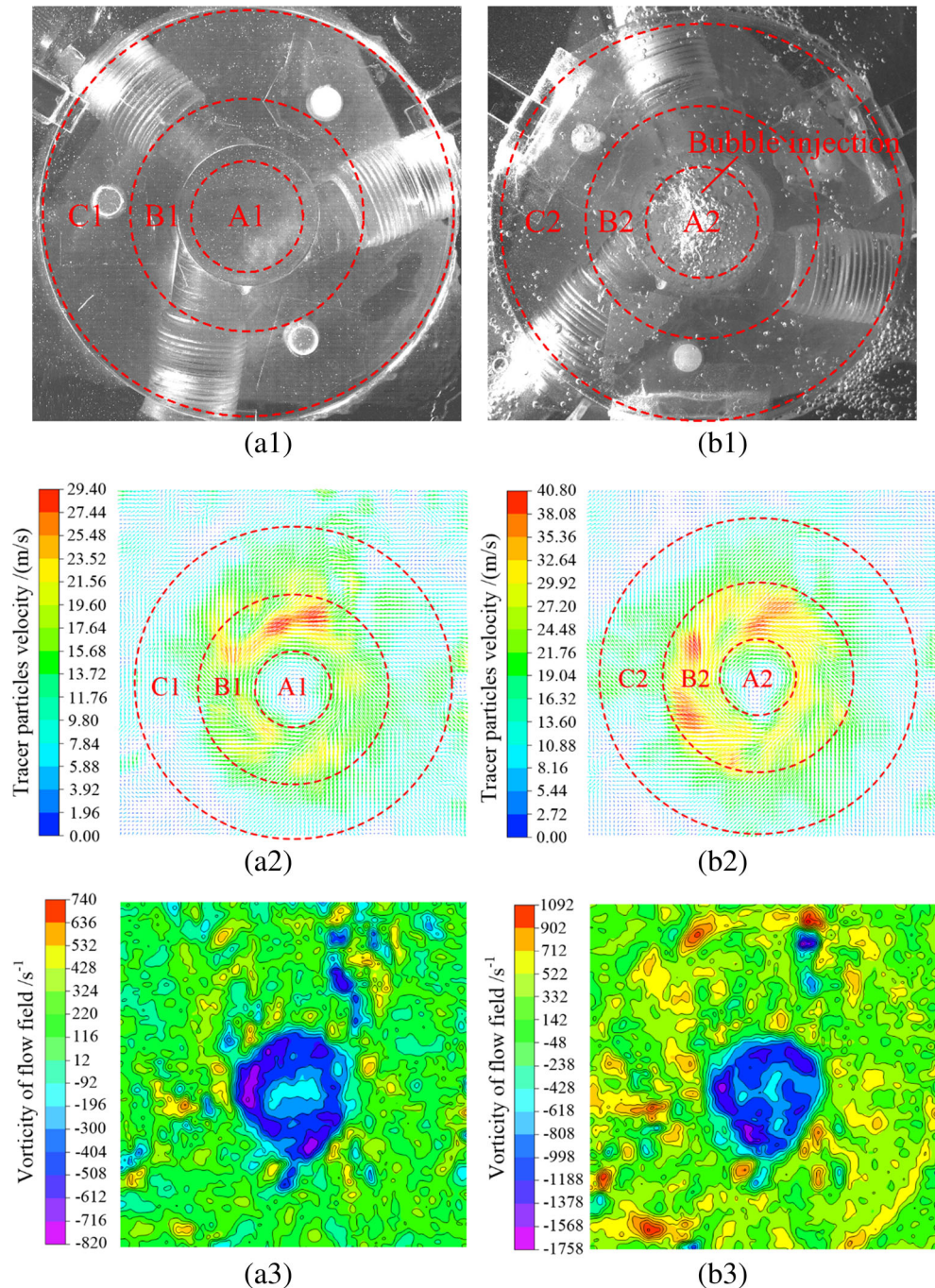
parameters of PIV apparatus are as follows: the trigger rate is 7 Hz, the time between pulses is 400 μs, and one-time acquisition includes 200 images.

The images of continuous 180 moments, that is, the time from 0 to 30 s, are analyzed by the vector analysis algorithms, and then the 180 velocity vector maps can be obtained. From the above-mentioned results, the average velocity vector fields can be acquired, as shown in Fig. 8a2, b2. Furthermore, the vorticity fields that can reflect the turbulent characteristics are acquired, as shown in Fig. 8a3, b3.

Figure 8a1–a3 describes the GLSP flow field without bubble injection, and Fig. 8b1–b3 shows the case with bubble injection. We can find that under the effect of multi-directional injection, low-velocity regions form the center of workpiece (regions A1 and A2), velocity enhancement regions that present circular shape can form (regions B1 and B2), and the variation regulars of the

above velocity vectors accord with the simulation results, as illustrated in Fig. 4b.

For the case without bubble injection, the velocity vector field can be divided into three regions: A1, B1, and C1. First, in the central region of flow field (region A1), a stable vortex with the lowest velocity is created, which can be regarded as a rigid core of Rankine vortex. Then, owing to the decrease in flow passage scale, the velocities arrive at the maximum amplitude in the initial constrained surface (region B1). It also can be noticed that the max velocity can reach approximately 29.4 m/s. Finally, the velocities decrease in the periphery flow field (region C1) under the effect of flow resistance.

The above-mentioned regulars also can be found in the case of bubble injection. Moreover, the following characteristics can be obtained from Fig. 8b1–b3: (1) The velocities are strengthened obviously under the acceleration effect of the injection bubbles, especially in the initial constrained surface

Fig. 9 Local front view of the GLSP flow field: **a1** Photograph without bubble injection. **a2** Instantaneous velocity vector field without bubble injection. **a3** Instantaneous vorticity field without bubble injection. **b1** Photograph with bubble injection. **b2** Instantaneous velocity vector field with bubble injection. **b3** Instantaneous vorticity field with bubble injection
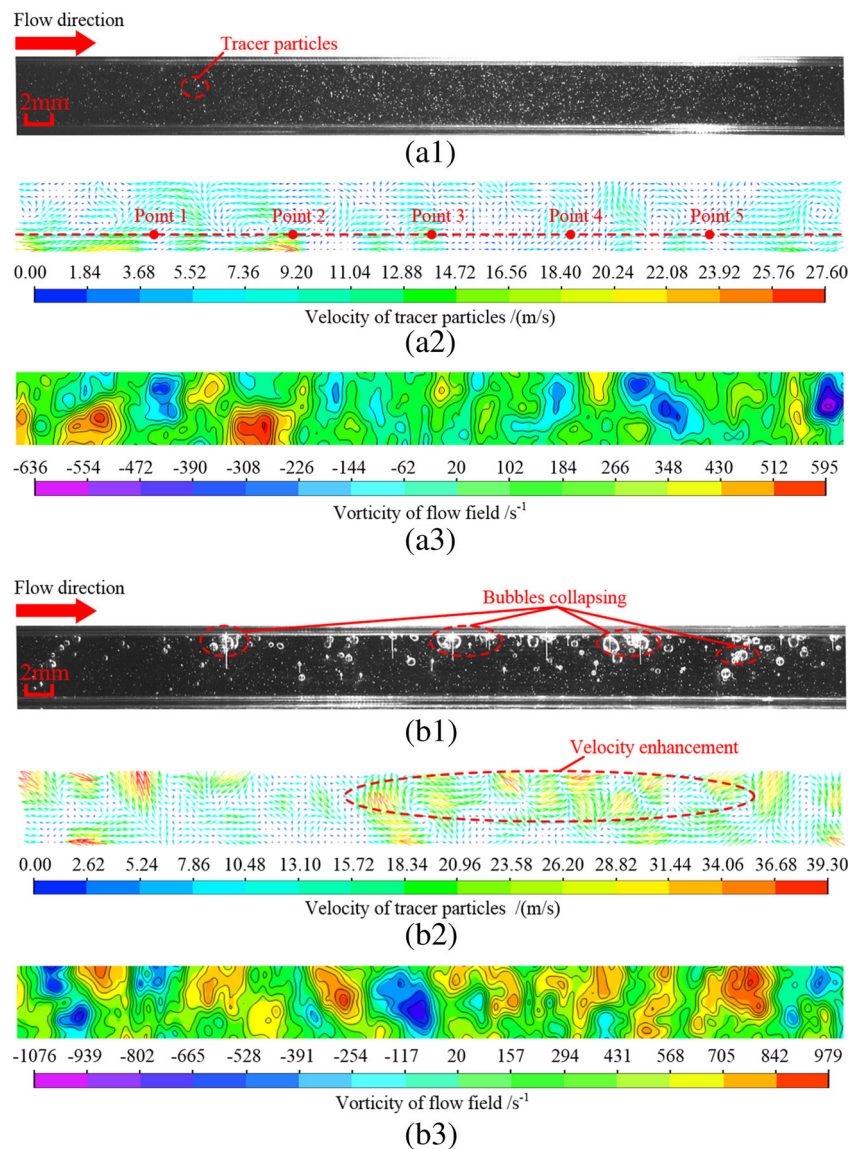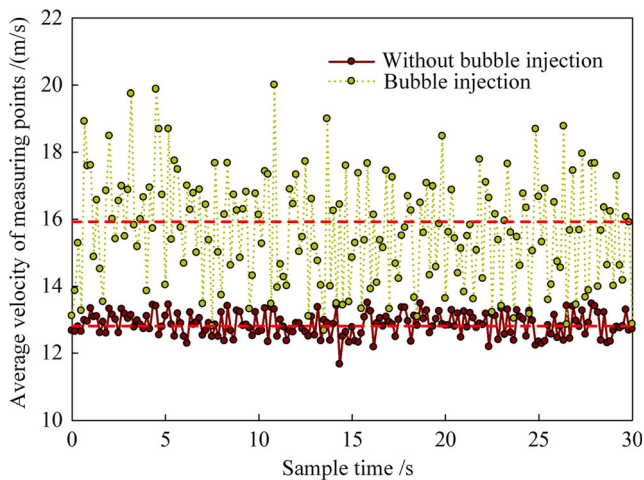
Fig. 10 Comparative results of average velocity variation

(region B2), and the maximum velocity can reach approximately 40.8 m/s. (2) From Fig. 8b1, we can find that the scales of the bubbles in region B2 are smaller than the scales of the bubbles in region B1. It indicates that the intensely collapsing happens here, which accords with the simulation results (Fig. 5f). (3) Vorticity is one of the most important physical quantities for describing turbulent vortex motion. Compared with the result in Fig. 8a3, the strength and breadth of vorticity in Fig. 8b3 are enhanced and the turbulent motion of tracer particles is intense.

To further illustrate the effects of bubble collapsing on the near-wall region, a rectangular channel for the cross section of constrained flow passage is constructed, as shown in Fig. 9a1, b1, and the comparative observation experiments under the conditions without and with bubble injection are also performed.

Figure 9a1–a3 presents the flow field state without bubble injection at 11.33 s, and we can obtain the following regulars.

(1) Given the existence of wall effect, the magnitude and direction of the near-wall particle velocities tend to be stable and the particle motion is ordered. The disordered motion of particles contributes to the processing uniformity of workpiece texture. Therefore, it is necessary to disturb the near-wall particle motion. (2) In Fig. 9a3, the velocity vortices randomly exist in the flow passage owing to the fluid turbulence effect, which illustrates that the surface constrained structure of the proposed processing tool can produce disordered processing effects.

Figure 9b1–b3 is one of the bubble collapsing moment (11.17 s), and the following regulars can be inferred. (1) Figure 9b1 shows that the bubbles mainly concentrate in the upper space of flow passage as a result of the low density. Therefore, the existence of bubbles will not obstruct the particle-wall collision. (2) As shown in Fig. 9b2, the velocities are enhanced under the effects of bubble collapsing (the maximum velocity can reach 39.3 m/s) and the directions are disordered. Moreover, the vortex motion of tracer particles becomes intense, as shown in Fig. 9b3. Apparently, the bubble collapsing is beneficial for improving the surface quality.

Furthermore, the statistical analysis of average velocity within the sample time is completed. First, five points are selected in the near-wall region, as shown in Fig. 9a2. Then, the average velocity of five points can be obtained and is plotted in the figure. Consequently, the average velocities of 180 continuous moments are calculated (the total time is 30 s, and the time interval is 0.17 s), and the results are shown in Fig. 10.

Obviously, the bubble injection can increase the tracer particles' velocities, and the average velocity of the total sample time increases from 12.90 to 15.97 m/s. In the case without bubble injection, the velocities of most moments range from 12.5 to 13.5 m/s. If the bubbles are injected, then this

Fig. 11 GLSP experimental platform. 1 Processing tool. 2 Flow meter. 3 Pressure meter. 4 Bubble flow. 5 Proportional valve. 6 Computer. 7 Bubble pump. 8 Self-priming pump. 9 Abrasive flow. 10 Abrasive flow container. 11 Workpiece
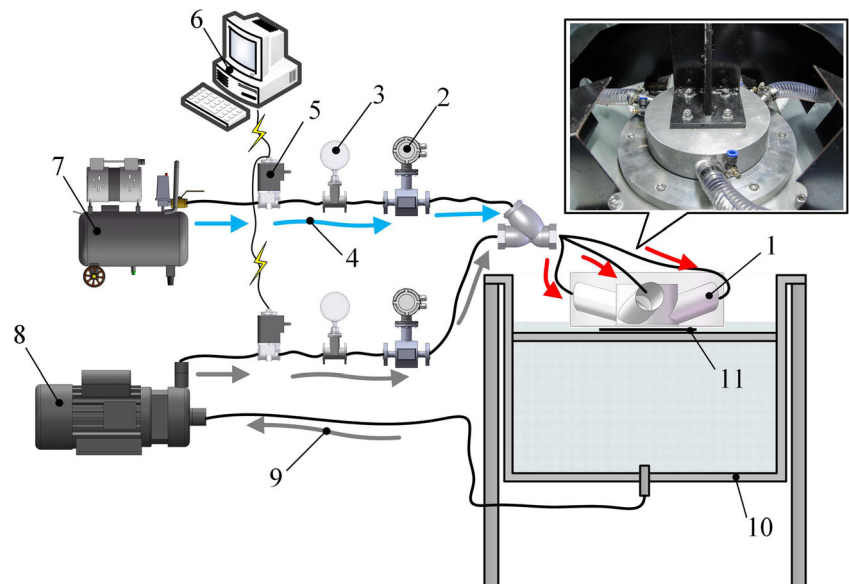
amplitude range increases to 15–17 m/s and the maximum velocity can reach approximately 20.00 m/s. Moreover, it can be noticed that the variation in velocity amplitude becomes intense, which indicates that the bubble collapse is chaotic, with positive effects to improve the processing uniformity. The above-mentioned statistical analysis reveals that the bubble collapsing can improve the processing quality and efficiency.

5 Processing experiments and result discussion

5.1 GLSP experimental platform

To check the effectiveness of the proposed method, a GLSP experimental platform is developed, as shown in Fig. 11. The processing workpiece is a silicon wafer with a diameter of 100 mm, and the processing experiment conditions are listed in Table 2.

First, the abrasive particles and deionized water are mixed in the abrasive flow container, and the SAF processing medium can be created (particle concentration is approximately 10%). Then, the SAF and bubble flow are respectively pumped into a three-way valve (gas volume fraction is approximately 15%). After being mixed together, the gas-liquid-solid three-phase abrasive flow is created and injected into the processing tool. The bubble and abrasive flow rates are controlled by the proportional valves.

5.2 Experimental result discussion

Based on the above experimental platform, two groups of comparative processing experiments are performed. The first group has no bubble injection, that is, the SAF processing method and the other is the GLSP method. According to the technical procedures for silicon wafer, the processing experiments include three stages: rough processing, semi-processing, and fine processing. For the first stage, 1500# SiO_2 particles are used to eliminate the machining marks with a processing time of 4 h. The second adopts 6000# SiO_2 particles, and the processing time is 8 h. Finally, 10000# SiO_2 particles are adopted to perform the final surface processing.

Table 2 Experimental conditions

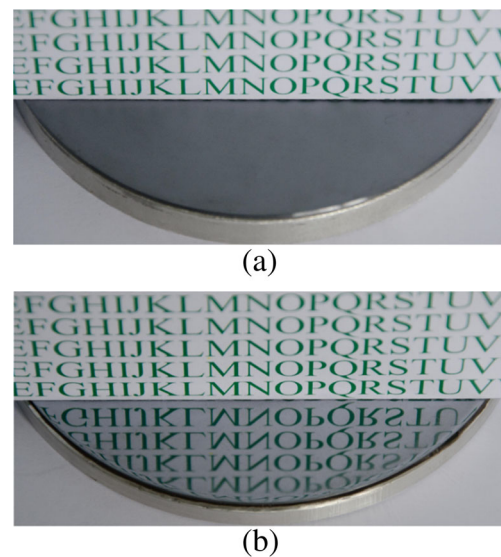| Experimental items	Experimental conditions
Material of workpiece	Silicon wafer; diameter = 100 mm
Self-priming pump	Power = 3 kW; flow rate = 25 m^3/h
Bubble pump	Power = 1.6 kW; flow rate = 7.2 m^3/h
Abrasive particle	SiO_2 = 1500#, 6000#, 10000#
Liquid medium	Deionized water

Fig. 12 The processed surface by the GLSP method. **a** Before processing. **b** After processing

Figure 12a shows the initial surface of silicon wafer, and Fig. 12b shows the surface after 28 h processing by the GLSP method. We can find that the workpiece can reflect clear image and has better uniformity.

Surface roughness and surface topography are the most basic technical parameters of surface quality. In order to observe the processing effects and validate the effectiveness of GLSP method, the eight measurement points are selected on the workpiece surface, as shown in Fig. 13.

Figures 14 and 15 show the surface roughness curves of the measurement points after 28 h processing, and the following regulars can be obtained. (1) The roughness variation curves decrease sharply first and then drop slightly to a stable roughness. (2) The bubble collapsing effects can be reflected in the rough processing stage, in which the proposed GLSP method only requires 4 h to reach the roughness of less than 100.00 nm, whereas the SAF method needs 8 h. (3) The final roughness processed by the GLSP method can reach 2.84 nm,
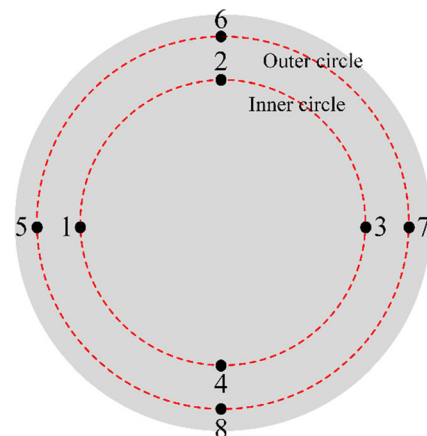

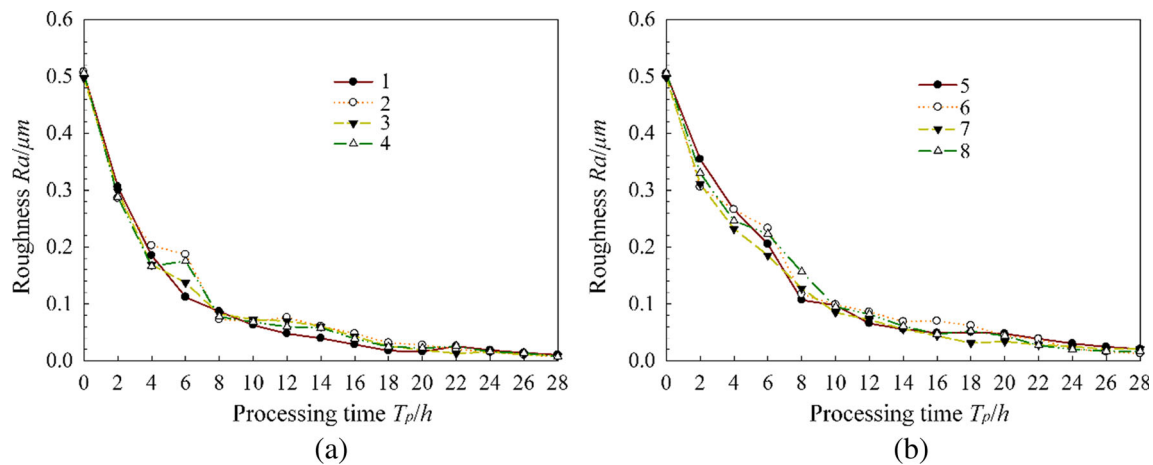**Fig. 13** The distribution of roughness measurement points

Fig. 14 Roughness variation curves of SAF method (first group). **a** The inner circle. **b** The outer circle

with roughness distribution of high uniformity; the final roughness processed by the SAF is 7.12 nm, with the need of much time to reach the same level. (4) In the first group of experiments, the roughness of inner circle decreases more rapidly than the roughness of outer circle; in the second group of experiments, the inner and outer circles can nearly reach the same roughness decrease rate. The aforementioned results prove that the bubble injection can expand the effective processing region of abrasive flow, thereby improving the processing efficiency and precision.

Another traditional method of processing the hard-brittle material is surface grinding. Many scholars have studied on it. According to their reports, the average surface roughness obtained by them is less than 10 nm (Ra = 6.60 nm) [33]. However, this is a tool-contact processing method, and it cannot be used to process the workpiece with complex geometric shapes. The processing conditions (such as wheel rotation speed, feed rate) must be controlled strictly to reduce the deep scratches and surface repeated damages [34]. GLSP method can process the workpiece with complex geometric shapes. Meanwhile, it is a fluid-based processing method, and the

fluid can buffer the over-impacting effects, thereby the surface damages can be reduced.

Figure 16 shows the 3D surface topography after 28 h processing, measured by a white light interferometer. Figure 16a1–a4 shows the surface topographies of points 1–4 processed by SAF. Figure 16b1–b4 shows the surface topographies of the same points processed by GLSP. From the figure, the following regulars can be obtained.

(1) The uniformity of workpiece surface texture processed by GLSP is better than the processing result of SAF, especially for the segment of point 1. (2) Compared with that of the SAF method, the GLSP method can obtain lower surface roughness (point 4: Ra = 2.84 nm). (3) In the second group of experiments, point 4 can reach the minimum roughness and the most uniform surface texture. Combined with the results in Figs. 4 and 5, it can be inferred that this phenomenon mainly caused by the difference in particle distribution and bubble collapsing distribution on the workpiece surface.

From the results in Figs. 8, 9, and 10 and 12, 13, 14, 15, and 16, we can find that the GLSP has better processing efficiency and precision than those of the SAF method. This superiority
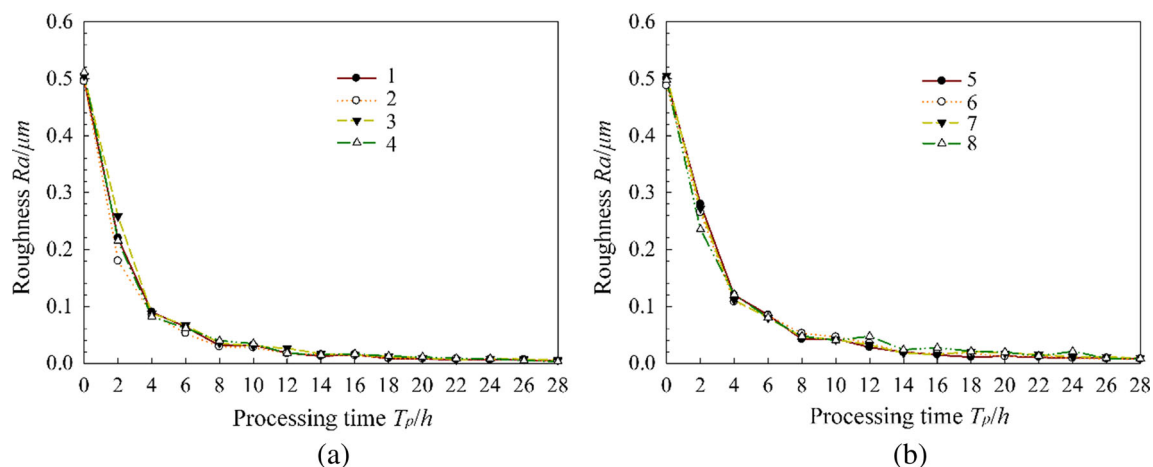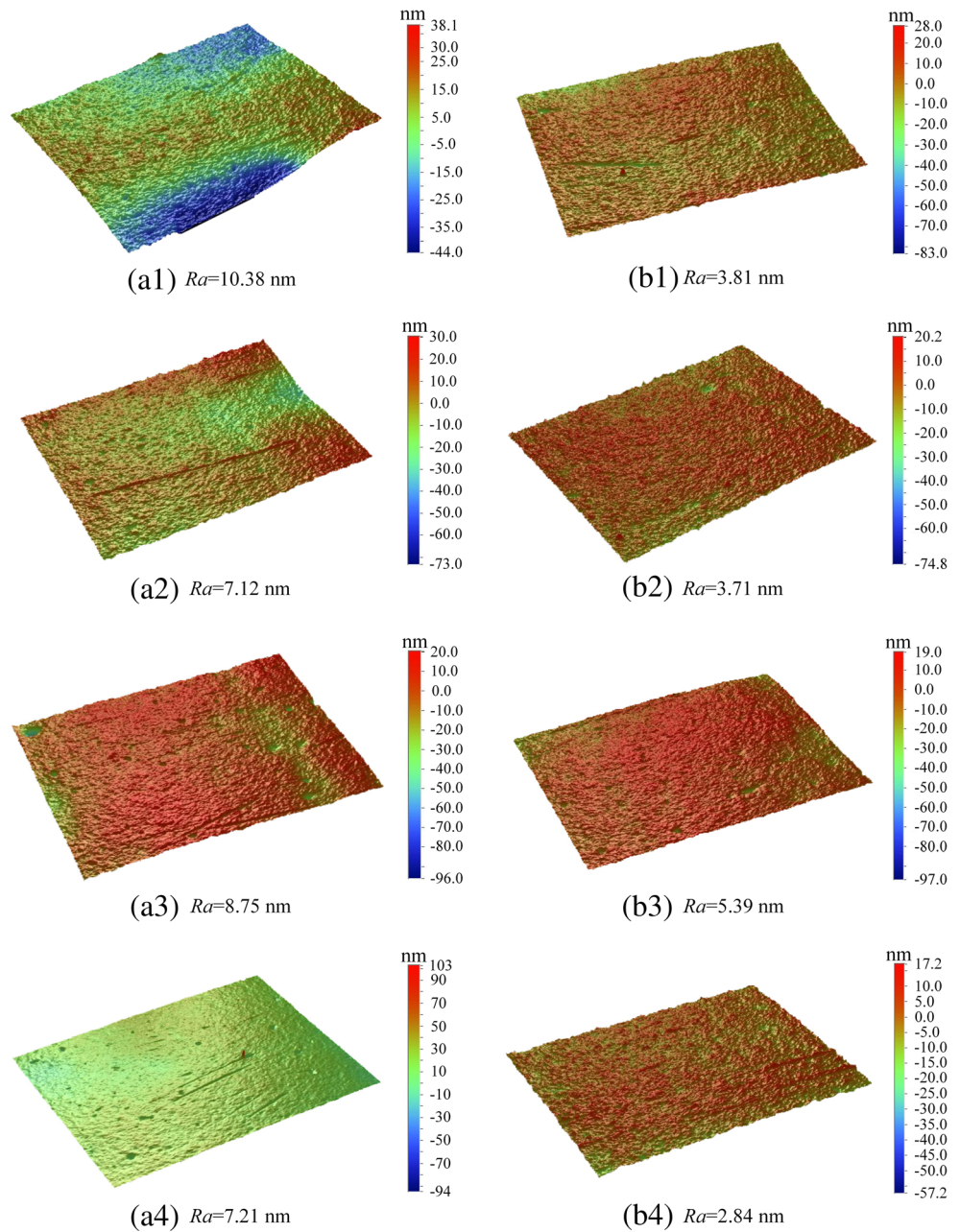

Fig. 15 Roughness variation curves of GLSP method (second group). **a** The inner circle. **b** The outer circle

Fig. 16 Surface topography data respectively obtained by SAF and GLSP method. **a1** First group point 1. **b1** Second group point 1. **a2** First group point 2. **b2** Second group point 2. **a3** First group point 3. **b3** Second group point 3. **a4** First group point 4. **b4** second group point 4

(a1) *Ra*=10.38 nm

(b1) *Ra*=3.81 nm

(a2) *Ra*=7.12 nm

(b2) *Ra*=3.71 nm

(a3) *Ra*=8.75 nm

(b3) *Ra*=5.39 nm

(a4) *Ra*=7.21 nm

(b4) *Ra*=2.84 nm

may be caused by the following fluid mechanic regulars. (1) The high-speed injection of bubble flow disturbs the particle aggregation phenomenon and improves the distribution uniformity of abrasive particles. (2) The effects of bubble collapsing can strengthen the particle kinetic energy and can induce disordered motion of the particles.

6 Conclusions

To address the low processing efficiency of SAF on hard-brittle materials, a GLSP method based on the bubble collapsing effects is proposed. The corresponding theoretical modeling and processing experiments are performed to achieve the research goals, and the main conclusions are as follows:

1. Based on the Euler multi-phase model, standard $k - \varepsilon$ turbulence model, and PBM model, a GLSP fluid mechanic model is built and the profiles of four key factors (granular pressure, particle dynamic pressure, particle turbulent kinetic energy, and particle volume fraction) of abrasive flow processing can be obtained. The results show that the effective processing region locates in the initial constrained surface. The bubble collapsing distributions show that the most violent collapses occur in the initial

constrained surface region, and it can improve the processing capability of abrasive particles in the effective processing region. Fluid viscosity apparently influences the processing characteristics of GLSP, and the fluid medium with low fluid viscosity can exert good processing effects.

2. To verify the effectiveness of the proposed method, the comparative observation experiments based on the PIV method are completed. This part includes two observation targets: global and local flow fields. By the global observation experiment, the instantaneous velocity vector field of GLSP can be obtained and the simulation results are validated. Through local observation experiment, the effects of the bubble collapsing on the near-wall region can be revealed and the observation results show that the average particle velocity counted in the total sampling time can increase from 12.90 to 15.97 m/s and that the maximum velocity can reach 20 m/s.

3. A GLSP experimental platform is developed, and the comparative processing experiments for silicon wafer are performed. The results show that the proposed GLSP method exhibits better processing efficiency and precision than those of the SAF method. The GLSP method only requires 4 h to reach a roughness of less than 100.00 nm, whereas the SAF method needs 8 h. After 28-h processing, the roughness processed by the GLSP method can reach approximately 2.84 nm, whereas the roughness processed by the SAF is 7.12 nm.

In general, the main contribution of this paper is introducing the bubble collapsing effects into the abrasive flow processing and providing an improved SAF method, that is, the GLSP method. Bubble collapsing can increase the particle kinetic energy and particle disordered motion. As a result, the processing efficiency and quality can be improved. This research not only can provide direct suggestions for the SAF method but also can offer a universal reference to the three-phase fluid mechanic modeling method for fluid-based processing methods. Subsequent research works will be performed on the mesoscopic dynamic modeling and multiphase abrasive flow energy transition mechanism.

References

1. Beaucamp A, Namba Y (2013) Super-smooth finishing of diamond turned hard X-ray molding dies by combined fluid jet and bonnet polishing. CIRP Ann - Manuf Techn 62(1):315–318

2. Zeng X, Li JH, Ji SM, Pan Y, Hang W, Chen GD (2017) Research on machining characteristic of double-layer elastomer in pneumatic wheel method. Int J Adv Manuf Technol 92(1–4):1329–1338

3. Guo DM, Liu JY, Kang RK, Jin ZJ (2007) A pad roughness model for the analysis of lubrication in the chemical mechanical polishing of a silicon wafer. Semicond Sci Tech 22(7):793–797

4. Zhang L, Wang JS, Tan DP, Yuan ZM (2017) Gas compensation-based abrasive flow processing method for complex titanium alloy surfaces. Int J Adv Manuf Technol 92(9–12):3385–3397

5. Li J, Ji SM, Tan DP (2017) Improved soft abrasive flow finishing method based on turbulent kinetic energy enhancing. Chinese J Mech Eng 30(2):301–309

6. Zeng X, Ji SM, Jin MS, Tan DP, Li JH, Zeng WT (2014) Investigation on machining characteristic of pneumatic wheel based on softness consolidation abrasives. Int J Precis Eng Manuf 15(10):2031–2039

7. Ji SM, Xiao FQ, Tan DP (2010) A new ultraprecision machining method with softness abrasive flow based on discrete phase model. Adv Mater Res 97-101:3055–3059

8. Zeng X, Ji SM, Jin MS, Tan DP, Ge JQ (2016) Research on dynamic characteristic of softness consolidation abrasives in machining process. Int J Adv Manuf Technol 82(5–8):1115–1125

9. Ji SM, Weng XX, Tan DP (2012) Analytical method of softness abrasive two-phase flow field based on 2D model of LSM. Acta Phys Sin 61(1):010205

10. Tan DP, Zhang LB (2014) A WP-based nonlinear vibration sensing method for invisible liquid steel slag detection. Sensor Actuat B - Chem 202:1257–1269

11. Tan DP, Ni YS, Zhang LB (2017) Two-phase sink vortex suction mechanism and penetration dynamic characteristics in ladle teeming process. J Iron Steel Res Int 24(7):669–677

12. Das M, Jain VK, Ghoshdastidar PS (2008) Fluid flow analysis of magnetorheological abrasive flow finishing (MRAFF) process. Int J Mach Tools Manuf 48(3–4):415–426

13. Jain VK, Adsul SG (2000) Experimental investigations into abrasive flow machining (AFM). Int J Mach Tools Manuf 40(7):1003–1021

14. Kanaoka M, Takino H, Nomura K, Mori Y, Mimura H, Yamauchi K (2007) Removal properties of low-thermal-expansion materials with rotating-sphere elastic emission machining. Sci Technol Adv Mat 8(3):170–172

15. Strnadel B, Hlavac LM, Gembalova L (2013) Effect of steel structure on the declination angle in AWJ cutting. Int J Mach Tools Manuf 64:12–19

16. Wang T, Cheng HB, Chen Y, Tam H (2014) Multiplex path for magnetorheological jet polishing with vertical impinging. Appl Opt 53(10):2012–2019

17. Ji SM, Li C, Tan DP, Yuan QL, Chi YW, Zhao LH (2011) Study on machinability of softness abrasive flow based on Preston equation. Chinese J Mech Eng 47(17):156–163

18. Ji SM, Xiao FQ, Tan DP (2010) Analytical method for softness abrasive flow field based on discrete phase model. Sci China-Technol Sci 53(10):2867–2877

19. Li C, Ji SM, Tan DP (2012) Softness abrasive flow method oriented to tiny scale mold structural surface. Int J Adv Manuf Technol 61(9–12):975–987

20. Zhang L, Deng B, Xie Y, Zhang R, Ji S, Wen D (2015) Curved surface turbulence precision machining method for artificial joint complex of titanium alloy. Mater Res Innov 19(S8):55–59

21. Tan DP, Ji SM, YZ F (2016) An improved soft abrasive flow finishing method based on fluid collision theory. Int J Adv Manuf Technol 85(5–8):1261–1274

22. Lehr F, Millies M, Mewes D (2002) Bubble-size distributions and flow fields in bubble columns. AICHE J 48(11):2426–2443

23. Wang TF, Wang JF, Jin Y (2003) A novel theoretical breakup kernel function for bubbles/droplets in a turbulent flow. Chem Eng Sci 58(20):4629–4637

24. Tan DP, Yang T, Zhao J, Ji SM (2016) Free sink vortex Ekman suction-extraction evolution mechanism. Acta Phys Sin 65(5): 054701

25. Zhang YL, Yeo KS, Khoo BC, Wang C (2001) 3D jet impact and toroidal bubbles. J Comput Phys 116(2):336–360

26. Ni BY, Zhang AM, Wang QX, Wang B (2012) Experimental and numerical study on the growth and collapse of a bubble in a narrow tube. Acta Mech Sinica-PRC 28(5):1248–1260

27. Chen JL, Xu F, Tan DP, Shen Z, Zhang LB, Ai QL (2015) A control method for agricultural greenhouses heating based on computational fluid dynamics and energy prediction model. Appl Energ 141: 106–118

28. Tan DP, Li PY, Ji YX, Wen DH, Li C (2013) SA-ANN-based slag carry-over detection method and the embedded WME platform. IEEE T Ind Electron 60(10):4702–4713

29. Zeng X, Ji SM, Tan DP, Jin MS, Wen DH, Zhang L (2013) Softness consolidation abrasives material removal characteristic oriented to laser hardening surface. Int J Adv Manuf Technol 69(9–12):2323–2332

30. Ramkrishna D, Mahoney AW (2002) Population balance modeling. Promise for the future. Chem Eng Sci 57(4):595–606

31. Luo H, Svendsen HF (1996) Theoretical model for drop and bubble breakup in turbulent dispersions. AICHE J 42(5):1225–1233

32. Fleischhauer E, Azimi F, Tkacik P, Keanini R, Mullany B (2015) Application of particle image velocimetry (PIV) to vibrational finishing. J Mater Process Tech 229:322–328

33. Biswas I, Kumar AS, Rahman M (2010) Experimental study of wheel wear in electrolytic in-process dressing and grinding. Int J Adv Manuf Technol 50(9–12):931–940

34. Luo SY, Chen KC (2009) An experimental study of flat fixed abrasive grinding of silicon wafers using resin-bonded diamond pellets. J Mater Process Technol 209(2):686–694